Available online at www.sciencedirect.com
SCIENCE DIRECT®
International Journal of Mass Spectrometry 244 (2005) 125–134
International Journal of Mass Spectrometry
www.elsevier.com/locate/ijms

Ion microprobe (NanoSIMS 50) Pb-isotope geochronology at <5 μm scale

Richard A. Stern [a,*], Ian R. Fletcher [a], Birger Rasmussen [b], Neal J. McNaughton [b], Brendan J. Griffin [a]

[a] *Centre for Microscopy and Microanalysis, M010, The University of Western Australia, Crawley, WA 6009, Australia*
[b] *School of Earth and Geographical Sciences, M006, The University of Western Australia, Crawley, WA 6009, Australia*

Received 14 April 2005; received in revised form 25 May 2005; accepted 25 May 2005

Abstract

Techniques have been developed for ion microprobe Pb-isotope dating of minerals at a lateral scale <5 μm using the Cameca NanoSIMS 50. Probe spots 3–5 μm in diameter comprising 16 keV $^{16}O^-$ ions were utilized in the analyses by magnetic peak-switching of $^{204}Pb^+$, $^{206}Pb^+$, $^{207}Pb^+$, and $^{208}Pb^+$ in NIST SRM 981 and 982 Pb metals, and ∼1 Ga uraninite, xenotime, and zirconolite reference materials. The Pb^+ mass resolution ($M/\Delta M$ at 1% peak height) was adjusted to ∼5000 to ensure the separation of molecular isobars. Under such conditions, the sensitivity for Pb^+ in zircon and zirconolite was 3.0–3.5 and ∼10 cps/ppm/nA $^{16}O^-$, respectively, about one-third the sensitivity obtained with large-geometry ion probes. Instrumental mass fractionation for Pb^+ was undetectable for SRM Pb metals and zirconolite, but values of up to 1.2% per atomic mass unit (enhancement of lighter isotopes) were recorded for xenotime and uraninite. As a demonstration of the technique, small zirconolite grains from a Cambrian mafic sill were analyzed in situ using a 3 μm diameter probe. A mean $^{207}Pb^*/^{206}Pb^*$ age of 504 ± 18 Ma was determined, and is considered an accurate measure of the crystallization age. Small-spot geochronology with the NanoSIMS at the present time is practical mainly for high-U mineral chronometers.

Keywords: Pb-isotopes; NanoSIMS; U–Pb geochronology; Ion microprobe; Instrumental mass fractionation

1. Introduction

The use of an ion microprobe to conduct analyses of mineral U–Th–Pb chronometers such as zircon was first reported by Andersen and Hinthorne [1] and detailed by Hinthorne et al. [2]. The relative success of this early ion microprobe dating stimulated the design of a large-geometry instrument (sensitive high resolution ion microprobe, 'SHRIMP') for which sensitivity and mass resolution were optimized specifically for the purposes of geochronology (e.g., [3]). The commercial versions of large-geometry instruments, particularly the SHRIMP II and Cameca IMS 1270/80, are now used routinely for U–Pb geochronology (e.g., [4]), employing O_2^- or O^- primary ion probe spots typically 10–30 μm in diameter, and with depth resolution of 0.1–1 μm.

Although many problems in U–Th–Pb geochronology can be addressed with these instruments, increasingly there is need to reduce the routine lateral sampling scale to <10 μm. Applications where improved spatial resolution is becoming increasingly necessary include the expanding field of in situ (i.e., from rock sections) dating. The mineral chronometers occurring in the rock sections may be extremely fine-grained, or have complex structural and chemical features, such as diagenetic minerals in sedimentary rocks [5–10], Ca–Zr–Ti oxides within some mafic igneous rocks [11], and metamorphic monazites (e.g., [12]). One approach to improve spatial resolution is the use of depth profiling, taking advantage of the superior depth resolution of the sputtering process (∼10–50 nm). Although depth profiling is an effective method for dating the outer crystal surfaces of concentrically

* Corresponding author. Tel.: +61 8 6488 8062; fax: +61 8 6488 1087.
E-mail address: rstern@cmm.uwa.edu.au (R.A. Stern).

1387-3806/$ – see front matter © 2005 Elsevier B.V. All rights reserved.
doi:10.1016/j.ijms.2005.05.005

zoned samples (e.g., [13–15]), it is not an in situ technique. The minerals of interest in the majority of cases are too texturally complex for depth profiling to be utilized; there is no practical alternative to analysis in section. A challenging goal for in situ analysis is to achieve useful age data at a sampling scale in which the lateral resolution matches the typical depth of sputtering, i.e., ~1 μm.

In this paper we present preliminary results of utilizing the small-spot capability of the Cameca NanoSIMS 50 ion microprobe to conduct Pb-isotope dating at the <5 μm lateral scale. We evaluate the sensitivity of the instrument for Pb secondary ions and the accuracy of the isotopic measurements through the analysis of various standard reference materials. The potential applications of the technology are illustrated by $^{207}Pb^*/^{206}Pb^*$ (where '*' denotes the radiogenic Pb) dating of a fine-grained igneous intrusive rock from Australia. Our evaluation of the instrument for Pb-isotope analysis provides the foundation for future developments involving calibration of the U–Pb and Th–Pb isotopic systems.

2. Analytical techniques

The NanoSIMS is a scanning ion microprobe possessing a double-focusing mass analyzer capable of high mass resolution and good transmission. The following text describes the instrument configuration (Fig. 1) and techniques relevant to its use for Pb-isotope analysis. The reader is directed elsewhere for a more general description of the instrument [16–18].

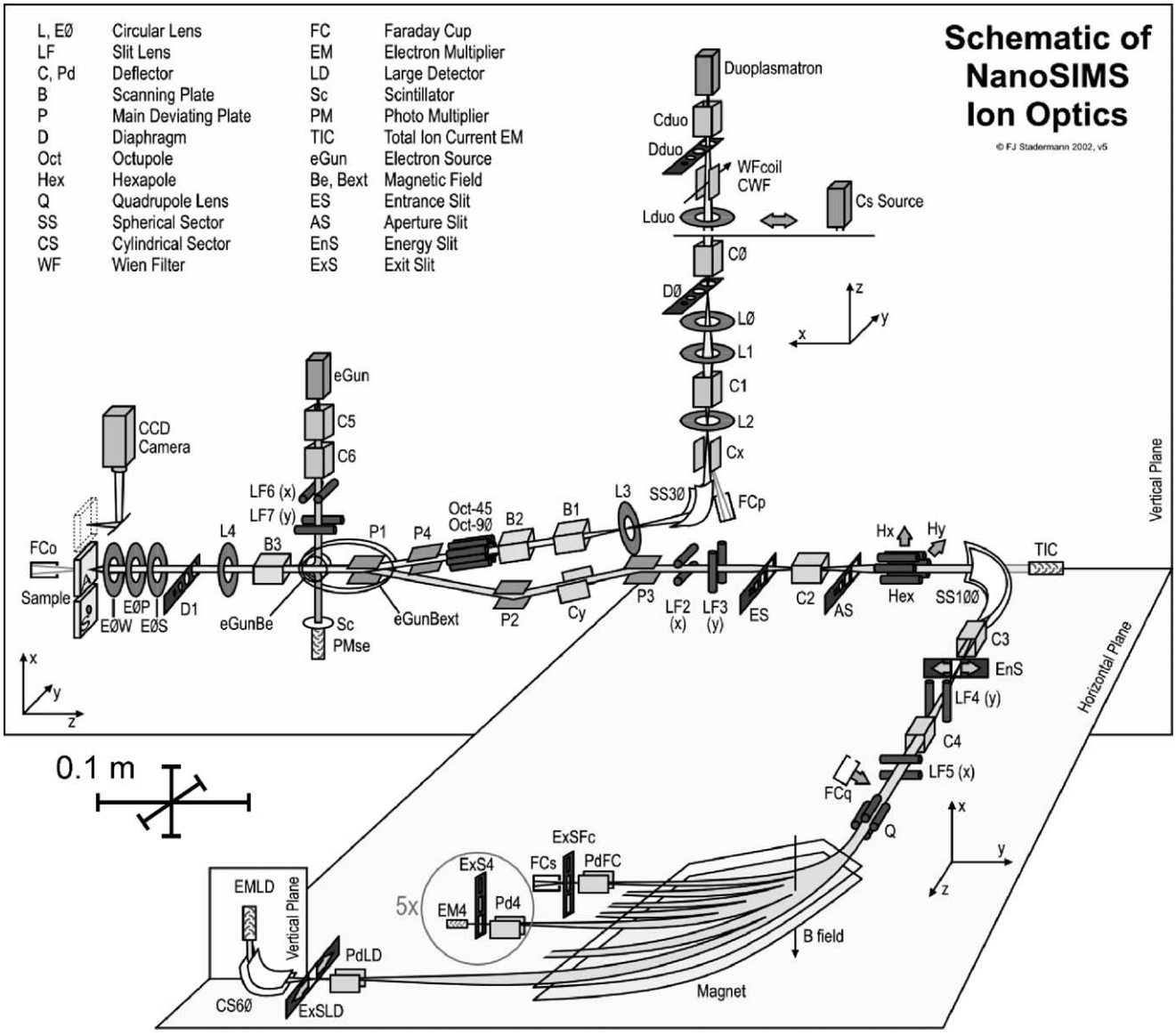

Fig. 1. Schematic diagram of the NanoSIMS 50 ion optics (Frank Stadermann, personal communication, 2005). Although not drawn to scale, approximate sizing is as indicated.

2.1. Oxygen probe

The primary column of the NanoSIMS (see Fig. 1) incorporates a duoplasmatron ion source in which the negative oxygen ions are accelerated through a potential of +8 kV, passed through a Wien velocity filter (for isolation of $^{16}O^-$), and focused to a spot on the target held at a positive potential of +8 kV, for a total impact energy of 16 keV. The primary oxygen probe size at the target is related to the diameter of the ion source object (real or virtual), the demagnification of the object onto the target surface, and ion beam aberrations. Currently, all ion microprobes use duoplasmatron ion sources of similar brightness, and the dominant factors that determine their ability to produce small probe spots of a given beam density are the spherical and chromatic aberrations of the final objective (condenser) lens system. These aberrations, particularly the spherical constant, increase proportionally with the focal length (i.e., working distance). Thus, in order to minimize aberrations, the focal length must be kept to a minimum [19]. For the conventional oxygen ion probes with separate beam paths for the primary and secondary ions, the minimum focal length is ~30 mm, but by combining the primary objective lens and the secondary extraction electrodes (coaxial configuration), both beam paths can be orthogonal to the sample surface, and the focal length can be reduced to ~5 mm [20]. The NanoSIMS ion probe incorporates the coaxial lens concept, and its focal length of 6 mm allows O-probe spots down to ~200 nm diameter to be achieved (but with only ~0.5 pA $^{16}O^-$).

The spot footprint for the NanoSIMS is largely determined by two apertures (D_0, D_1 in Fig. 1), and a fixed-diameter (2.5 mm) differential pumping tube just after D_0. An image of the ion source is focused at the D_0 aperture, located just downstream from the Wien filter, and D_0 acts as a real object for the primary column. A lens (L_0) between D_0 and the differential pumping tube controls the demagnification of D_0 and thus the beam current in the probe. Within the coaxial immersion lens near the target (combination of EOW, EOP, EOS and L4 in Fig. 1), the D_1 aperture controls the beam diameter at the target by limiting beam divergence and thus the spherical and chromatic aberrations originating within the final objective (EOP) lens.

The primary ion focusing results in an approximately Gaussian density distribution at the target (i.e., critical illumination), and it is common to utilize the knife-edge method to determine lateral resolution. Typically the linear distance between the 16 and 84% relative intensity measurements is chosen, encompassing 68% of the beam flux, however, according to IUPAC guidelines [21], the 16–84% definition is valid only for qualitative analysis. For quantitative analysis, the recommendation is a definition whereby the signal has diminished to 10^{-4} of its peak value, which is ~4σ in width. This definition provides a more realistic assessment of the spot size for the spatially sensitive measurements required of Pb-isotopic analysis in complex targets, where the tailing of the primary beam usually cannot be ignored.

The knife-edge method is time-consuming to carry out and requires specialized samples. Furthermore, it is not possible to directly view the sputtering site with incident light (see Section 2.4). Accordingly, we found that the most convenient and interactive method to tune and evaluate the spot footprint was to sputter a spot on any fresh area of the sample mount, waiting until the total secondary ion emission from the substrate stabilized (usually ~30 s, following sputtering through the Au layer), and then immediately conducting scanning total secondary ion imaging (TIC, Fig. 1) of a 10 μm × 10 μm area centered on the spot. The spot mark was then visible, as its secondary ion emission was much higher than the surrounding surface, and footprint measurements could be made on the imaging screen. The true size of the probe was smaller than measured (by about one-third) because the probe was being used to image itself. Nevertheless, the method did provide a rapid way to evaluate the effects of any primary beam tuning modifications. Subsequent to analysis, the true lateral resolution was determined from scanning secondary electron microscope images of the analysis pits generated by extended sputtering (~1 h). We estimate that the widths reported here are ~3σ, i.e., encompassing ~99% of the beam flux.

A combination of D_0 = 100 μm and D_1 = 200 μm (diameters), and tuning of L_0 and other lenses in the primary column (Fig. 1), produced spots that were 3–5 μm diameter (e.g., Fig. 2), with a typical total O^- current of 125–150 pA. The beam density was about 15 pA $O^-/\mu m^2$, a value that is within the range obtained for the large ion microprobes (10–50 pA $O^-/\mu m^2$). The sputtered pits were found to be elongate in plan rather than circular, due to astigmatism that was not correctable with the octupole stigmators (Oct-45 and Oct-90, Fig. 1). The probe asymmetry is thought to originate from a slight misalignment of the coaxial lens assembly. Although these conditions produced spot sizes that were an order of magnitude worse that the resolution for the instrument, they were chosen for this initial study in order to maximize beam

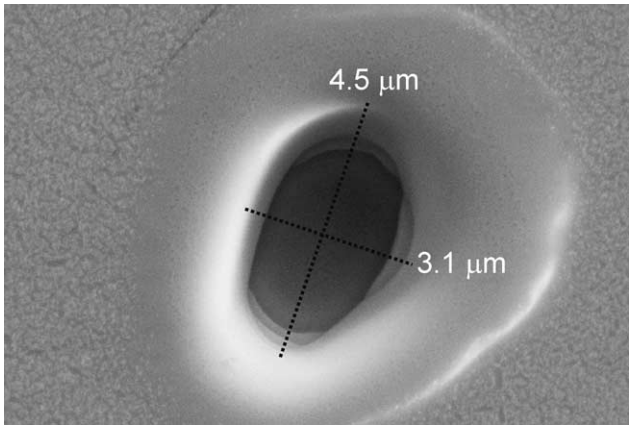

Fig. 2. Scanning electron microscope image of a sputtered crater in the mineral zirconolite made by ^{16}O-ion sputtering over ~1 h, with beam strength ~150 pA. The spot widths indicated are believed to encompass ~99% of the beam flux. The depth is estimated to be ~1 μm. The speckled texture surrounding the pit is the conductive Au coating.

currents, while remaining an improvement over existing standards of probe dimensions used in geochronology.

2.2. Mass analyzer

The surface of the target experiences a strong electrostatic extraction field (∼20 kV/cm), and 8 keV positive secondary ions are extracted and focused onto a fixed-width analyzer entrance slit (ES, Fig. 1). In this study, the smallest ES (10 μm) was utilized. The analyzer in the N50 is of Mattauch-Herzog geometry, with a 90° spherical ESA of 100 mm radius and an asymmetrical magnet permitting ion path radii between 145 and 550 mm. The magnification of the system (entrance to exit slit) is 0.644 at a magnet radius of 350 mm. Secondary ion losses at the ES (10 μm) are about 60% (relative to full transmission without slits), about 10% at the aperture slit (AS, Fig. 1), and 10% at the high energy slit (EnS, Fig. 1) that is used to reduce chromatic aberration. Accordingly, the net relative transmission at high resolution is ∼20%. Using a standard zircon reference material, the practical sensitivity for Pb^+ under these conditions was 3.0–3.5 cps/ppm (wt.)/nA O^-.

The detection electronics permit up to five secondary ion species to be simultaneously analyzed using discrete-dynode-type (Hamamatsu, Cu–Be) electron multipliers, four of which are moveable along the focal plane. However, the minimum mass separation for our instrument is ∼M/30, and consequently the Pb-isotopes required analysis by magnetic peak-switching. The detector chosen in this study, EM1 set at a radius of ∼450 mm, was selected based upon its superior pulse height distribution characteristics. Detection system deadtime was electronically fixed at 44 ns.

A fixed exit slit width of 25 μm was utilized, and in combination with a 10 μm entrance slit, a mass resolution, R, ($M/\Delta M$, peak width at 1% peak height definition) of 5000 ± 400 was obtained after appropriate tuning. An example of one of the best mass scans obtained for ^{206}Pb in xenotime is shown in Fig. 3, illustrating complete separation from molecular isobars. A flat peak top was present, with width from 40 to 60 ppm (mass). Cameca's 'mass resolving power' parameter (MRP) varied from 10,000 to 14,000 ($M/\Delta M$, where ΔM is width of the peak flank between 10% and 90% of peak height). The MRP is a measure of the relative width of the mass-resolved ion beam, but by itself MRP is insufficient to characterize the actual separation of peaks in a given experimental setup.

2.3. Secondary ion detection

A prerequisite for measuring accurate Pb-isotopes by peak hopping is ensuring that the electron multiplier (EM) is operating in such a state that the pulse height distribution (PHD) is well-defined (good resolution) and as robust as possible, i.e., there is minimum sensitivity to the position of the ion impact on the conversion dynode, ion energy, ion mass, etc. Minimizing variations in conversion dynode sensitivity

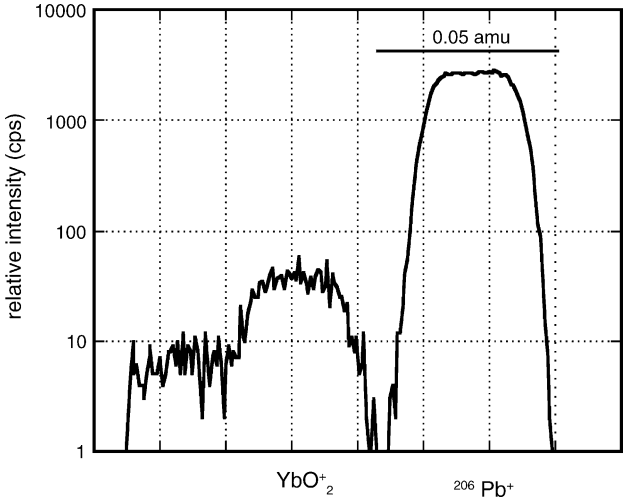

Fig. 3. NanoSIMS mass spectrum in the vicinity of m/e = 205.97 u in xenotime standard z6413. Mass resolution for $^{206}Pb^+$ = 5350, mass resolving power = 14,300, under operating conditions outlined in Section 2.2.

was found to be particularly important, as the mass-resolved $^{206}Pb^+$ beam was particularly narrow in this study (8–10 μm width at the exit slit, but larger at the first dynode), and thus any spatial variations in dynode sensitivity are highlighted. Cameca's guidelines for setting the key EM parameters for the NanoSIMS, i.e., multiplier voltage and threshold, hinge upon analysis of the PHDs, which are readily obtained by stepping the threshold while monitoring the signal intensity at a constant voltage [22]. The PHD profiling must be repeated to evaluate the effects of varying the voltage, and similarly for variations in the position of the beam on the conversion dynode.

We used a combination of approaches to facilitate arriving at appropriate EM conditions. Firstly, a typical threshold was selected based on previous experience with the detector (e.g., −75 mV), and the EM voltage manually stepped while recording the output of a constant signal ('gain' curve, Fig. 4a). The voltage was set at the lowest acceptable value on the characteristic plateau, where space-charge effects lead to the most robust PHD's. Then the PHD profile was determined, and if the PHD resolution was as recommended by Cameca, the threshold value was set according to guidelines. If the threshold was significantly different from the previous value, the gain curve was redrawn, and the calibration processes repeated. If, however, the PHD resolution was not as recommended, the beam was electrostatically deflected, using plates immediately in front of the exit slit, to another part of the dynode, and the processes repeated. Finally, the Pb^+ peak shape was determined by electrostatic deflection, as a final check of conversion dynode heterogeneity. Normally, with the multiplier voltage set appropriately, a flat-topped peak was demonstrated (Fig. 4b), but the effects of dynode heterogeneity are clearly revealed at sub-optimal voltages, as illustrated by the sloped peak top in Fig. 4c.

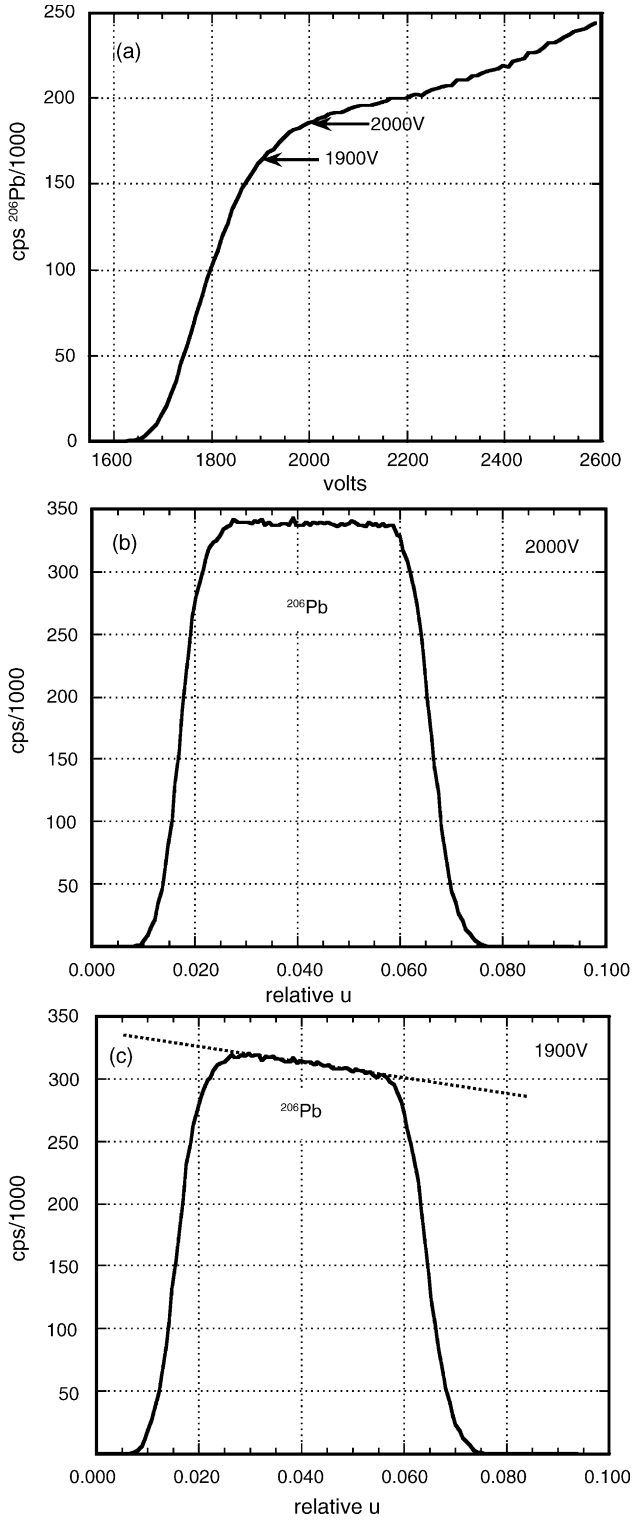

Fig. 4. (a) Gain plot (i.e., voltage vs. count rate) for $^{206}Pb^+$ in uraninite z6897, for the discrete-dynode Cameca-Hamamatsu electron multiplier used in this study. The threshold was set to −120 mV; (b) Corresponding $^{206}Pb^+$ peak shape for uraninite z6897 at optimal (2.0 kV) EM voltage; the mass resolution was relaxed (20 μm entrance slit, 50 μm exit slit, $R = 3010$) to permit better assessment of the peak top. (c) Corresponding $^{206}Pb^+$ peak shape at sub-optimal EM voltage (1.9 kV), showing sloped peak top largely due to lateral variations in conversion dynode PHDs (see text). Abbreviation: u = atomic mass unit (amu).

2.4. Sample targeting

The NanoSIMS does not allow one to view an optical image of the sample surface in the analysis position. Instead, the sample is first viewed in reflected light by CCD camera in a remote position to locate the region of interest (ROI), and then translated back to the analysis position. The reproducibility of this translation was ∼10 μm, which was insufficiently precise for locating particularly small ROIs. In such cases, the approach was to initially move to a location ∼50 μm away from the ROI, and raster the primary beam to remove the surface Au in a 10 μm × 10 μm patch. The rastered patch was subsequently identifiable by its strong total secondary ion emission compared with the adjacent Au-coated surface, and became an absolute reference marker on return to any region near the ROI. The sample was then translated to the CCD camera position, and the position of the raster patch relative to the ROI was quantified. The sample was returned to the analysis position, the characteristic raster patch located by scanning (total secondary) ion imaging, and the stage moved precisely to the ROI according to the vector determined from the reflected light image. For particularly small ROIs, it was further necessary to conduct scanning (mass-resolved) ion imaging utilizing $^{206}Pb^+$ (EM1), $^{248}ThO^+$ (EM3), or $^{270}UO_2{}^+$ (EM5) to identify the outlines of particular U–Th–Pb minerals [23].

2.5. Data acquisition

The Pb^+ beams were successively directed into the EM by magnetic field switching in an up-mass sequence. Hysteresis in the magnetic field control (Hall effect probes) required careful attention to calibrating the magnetic field prior to an analytical session, and this was accomplished using a common Pb standard (Pb-feldspar or Pb metal). Initially, the magnet field settings for each Pb peak position were determined manually, and then the magnetic field was cycled for several tens of minutes. Sometimes it was necessary to fine-tune the magnetic field settings at this point and repeat the cycling warm-up. Subsequently, precise peak centering for the setup standard was done automatically using electrostatic deflection. We experimented with magnetic field peak centering, which utilizes deviations in electrostatic centering voltages to calculate the required magnetic field adjustments, but concluded that this method was not as reliable for the narrow peaks in this study. For the analysis of common Pb, electrostatic peak centering was carried out for all Pb^+ peaks on the first cycle and every fifth cycle thereafter. For the analysis of minerals with low $^{204}Pb^+$, the $^{206}Pb^+$, $^{207}Pb^+$, and $^{208}Pb^+$ peaks were centered electrostatically, whereas the change in the deflections applied to $^{204}Pb^+$ were those determined for the previous measurements of $^{208}Pb^+$. Background position was set at $^{204}Pb^+ + 0.05$ amu, and also referenced to $^{208}Pb^+$.

A complete analysis consisted of rastering the probe in a square pattern to remove surface contaminants, secondary ion

tuning to maximize $^{206}Pb^{+}$, and then an analysis comprising 25 cycles through the four peaks and background position. An analysis lasted 20–40 min, depending on the nature of the target, and in some cases was repeated at the same location ('replicate'). Raw data were processed off-line, first using customized spreadsheets to reformat the data and correct for deadtime, and then using the SQUID U–Pb data processing platform [24] for calculation of raw data ratios and common Pb corrected ratios (using common Pb compositions from [25]), and $^{207}Pb^{*}/^{206}Pb^{*}$ ages, with statistically robust uncertainties.

3. Samples

Mineral grains were cast in 1 cm diameter low-outgassing resin (either Korapox® or Araldite 502) resin plugs, and progressively polished to 0.1 μm with diamond compound. Plugs (3 mm diameter) from thin-sections were also mounted in resin, and both types of samples evaporatively coated with ~20 nm of Au. Samples of Pb metal were cold pressed into indium and were left uncoated. Minerals were imaged using backscattered and secondary electron signals utilizing JEOL 6400 and Zeiss Supra 55VP scanning electron microscopes.

Four NanoSIMS mounts (NM#s) were prepared containing several types of reference materials whose Pb-isotopic compositions have been determined by thermal ionization mass spectrometry or SHRIMP II ion microprobe. These individual mounts were together installed within an eight-position mount holder for subsequent analysis. In addition, a fifth mount was prepared (NM62) from thin-sections of mafic rock from the Upper Cambrian-Lower Ordovician Table Hill Volcanics, South Australia [26].

3.1. Mount NM11

The pure Pb metal standards SRM 981 and 982 [27] have reference values as follows: for SRM 981, $^{208}Pb/^{206}Pb = 2.1677$, $^{207}Pb/^{206}Pb = 0.91489$, $^{204}Pb/^{206}Pb = 0.059030$, and for SRM 982, $^{208}Pb/^{206}Pb = 1.00016$, $^{207}Pb/^{206}Pb = 0.467080$, $^{204}Pb/^{206}Pb = 0.027212$ ([28], Table 6 in [29]).

3.2. Mount NM42

Fragments of the uraninite (UO_2) standards z6893 and z6897 ($^{206}Pb^{*}$ ~12 wt.%) have mean $^{207}Pb^{*}/^{206}Pb^{*} = 0.07219 \pm 0.00013$ (2σ) and 0.07446 ± 0.00017, respectively ([30] and unpublished data). Xenotime (YPO_4) z6413 ('XENO1'), containing 200–1000 ppm (wt.) $^{206}Pb^{*}$, has a mean $^{207}Pb^{*}/^{206}Pb^{*} = 0.072381 \pm 0.000029$ [31].

3.3. Mount NM56

Zirconolite ($CaZrTi_2O_7$) 'SRZL' comprised grains exposed in thin-section from a previous SHRIMP study (UWA mount 04–07) in which the mean SHRIMP $^{207}Pb^{*}/^{206}Pb^{*} = 0.08086 \pm 0.00012$, and Pb^{*} ~150–300 ppm [11].

3.4. Mount NM57

Zirconolite 'Z4' is a Sri Lankan megacryst (Z4-SL3-12) reported to have a bulk $^{207}Pb^{*}/^{206}Pb^{*} = 0.05034 \pm 0.00008$, and $^{206}Pb^{*}$ ~3300 ppm [32].

3.5. Mount NM62

The Table Hill Volcanics rock sample (TH1) is a late-stage, evolved dolerite (diabase) lithology taken from the Nyaninya sill, obtained from a surface outcrop located at Australian Map Grid coordinates 7406548N, 287374E. The sills are considered to be part of a ~500 Ma period of Australia-wide mafic magmatism, and a K–Ar age on plagioclase from one sample yielded a minimum crystallization age of 500.1 ± 7.4 Ma ([33] p. 4). Thin-sections were found to contain rare zirconolite grains intergrown with matrix feldspar, quartz, and chlorite. The zirconolite occurs as anhedral to euhedral grains, <50 μm in the largest dimension, and is typically bladed, with a thickness of <3 μm. It is variably affected by patchy secondary alteration. Zirconolite-baddeleyite (ZrO_2) intergrowths also occur.

4. Results and discussion

4.1. Standards

A summary of the isotopic results for the reference materials is presented in Table 1. Reported are the mean Pb-isotopic ratios, the reference values (as detailed above), and the calculated instrumental mass fractionation (IMF) for Pb, reported as deviations in % from the reference value per atomic mass unit, u, i.e., $IMF = 100 \cdot (R_m/R_s - 1)/(M_2 - M_1)$, where $M_{1,2}$ are nominal masses, R_m is the measured ratio (M_2/M_1), and R_s is the corresponding ratio of the standard. In this classic form of linear mass fractionation [34], IMF values are negative for the generally expected enhancement of the lighter isotopes in SIMS (e.g., [35]). In calculating the uncertainties in IMF, only the uncertainties in the NanoSIMS analyses are propagated.

The mean IMF values calculated for $^{208}Pb/^{206}Pb$, $^{207}Pb/^{206}Pb$, and $^{204}Pb/^{206}Pb$ ratios of the various Pb standards (Table 1) are plotted in Fig. 5. The data for the SRM standards are uncorrected for common Pb, as are the data for z6897 uraninite for which no ^{204}Pb was measured. The other data for minerals were corrected for common Pb using measured ^{204}Pb. The weighted mean IMF of all data is -0.11 ± 0.16%/amu (2σ, MSWD = 2.1). The data for SRM 981 Pb metal provided the most robust estimate of IMF, with the mean IMF derived from all three Pb ratios = 0.02 ± 0.13%/amu (MSWD = 0.25). Only two data

Table 1
NanoSIMS Pb-isotopic data for reference materials

Sample	Ratio type	Measured ratio	±2σ	Reference value	IMF (%/amu)	±2σ	N	MSWD	Median $^{204}Pb/^{206}Pb$	Median $^{208}Pb/^{206}Pb$
Metals										
SRM981	$^{204}Pb/^{206}Pb$	0.05892	0.00058	0.05903	0.09	0.98	7	4.30		
SRM981	$^{207}Pb/^{206}Pb$	0.9148	0.0013	0.91489	−0.01	0.14	7	1.03		
SRM981	$^{208}Pb/^{206}Pb$	2.1604	0.0099	2.1677	−0.17	0.46	7	1.70		
SRM982	$^{204}Pb/^{206}Pb$	0.02729	0.00015	0.02721	−0.14	0.55	2	0.00		
SRM982	$^{207}Pb/^{206}Pb$	0.4669	0.0017	0.46708	−0.04	0.36	2	0.43		
SRM982	$^{208}Pb/^{206}Pb$	0.9941	0.0024	1.00016	−0.30	0.24	2	0.13		
Minerals[a]										
Uncorrected for common Pb										
SRZL zrclt	$^{207}Pb/^{206}Pb$	0.08138	0.00081	0.08086	0.64	1.00	7	0.21		
Z4 zrclt	$^{207}Pb/^{206}Pb$	0.05839	0.00050	0.05834	0.09	0.86	5	2.70		
6893 uran	$^{207}Pb/^{206}Pb$	0.07176	0.00027	0.07219	−0.60	0.38	12	6.10		
6897 uran	$^{207}Pb/^{206}Pb$	0.07459	0.00025	0.07445	0.19	0.34	5	0.82		
6413 xeno	$^{207}Pb/^{206}Pb$	0.07198	0.00064	0.07238	−0.55	0.89	9	2.20		
Common Pb corrected (using ^{204}Pb)[b]										
SRZL zrclt	$^{207}Pb^*/^{206}Pb^*$	0.08059	0.00093	0.08086	−0.33	1.15	7	0.14	4.9E-05	1.09
Z4 zrclt	$^{207}Pb^*/^{206}Pb^*$	0.05829	0.00044	0.05834	−0.09	0.75	5	2.10	6.5E-06	0.065
6893 uran	$^{207}Pb^*/^{206}Pb^*$	0.07168	0.00030	0.07219	−0.71	0.42	12	5.40	5.7E-06	0.025
6413 xeno	$^{207}Pb^*/^{206}Pb^*$	0.07150	0.00079	0.07238	−1.22	1.10	9	3.50	2.0E-05	0.055

[a] Abbreviations—zrclt: zirconolite; uran: uraninite; xeno: xenotime.
[b] Corrected for common Pb at the accepted age and composition of [25].

(6893 uraninite, 6413 xenotime) are significantly non-zero, falling at negative IMF values (−0.7 and −1.2%/amu, respectively).

Based on these results, and giving most weight to the Pb metal standards, we see no evidence for significant bias to the Pb-isotope ratios. Nevertheless, the mean IMF value suggests a slight tendency to negative values (ca. −0.1%/amu). All the common Pb-corrected mineral data plot at negative IMF values, and the data for 6893 uraninite and 6413 xenotime are anomalously low. For these two samples, the IMF values remain negative (both −0.6%/amu) without common Pb correction (Fig. 5), indicating that an inaccurate common Pb correction could not be solely responsible for their negative IMF values. The possibility exists that the mineral grains and regions analyzed did not have the assumed isotopic compositions (i.e., are isotopically heterogeneous). Alternatively, there exists the possibility for bias in the Pb-isotope ratios due to the position of the mounts within the instrument. These two mineral samples were on the same mount (NM42), at a unique position on the multiple-mount holder compared to the other samples.

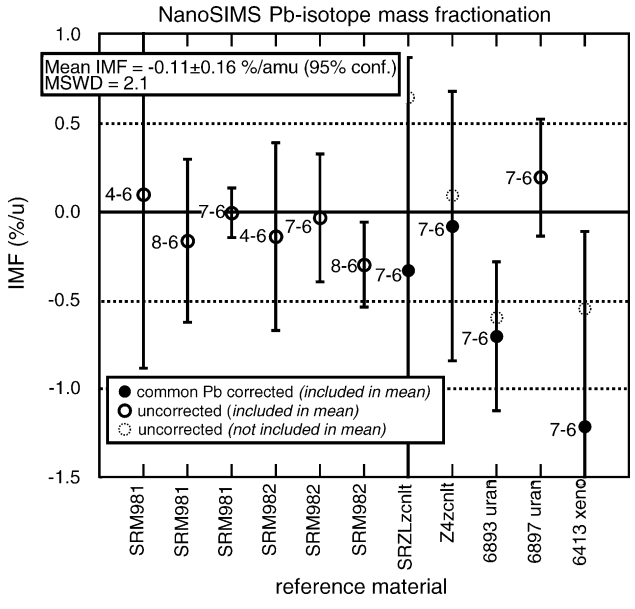

Fig. 5. NanoSIMS instrumental mass fractionation (IMF) for different Pb-isotope ratios ('4–6' is $^{204}Pb/^{206}Pb$, etc.) obtained for various reference materials (Table 1). Open circles are the mean IMF values without correction for common Pb. Filled circles are the mean IMF values for common Pb-corrected ratios. Error bars are 2σ, and where open and filled circles are both present, the uncertainty refers to the filled circle.

The results for the Sri Lankan Z4 zirconolite, whose bulk Pb composition is known (see above), indicate that $^{206}Pb^+$ sensitivity was ∼10 cps/ppm/nA $^{16}O^-$. This value is about 3× greater than determined for $^{206}Pb^+$ in zircon under similar conditions, and is consistent with previous reports on the relative ion yields of these two minerals using O_2^- primary ions [11].

4.2. Table Hill zirconolite

Pb-isotope data for sample TH1 were acquired from five spots on five separate zirconolite grains (Table 2 and Fig. 6). Due to the relative imprecision of the sample stage travel over long distances, and the absence of reflected light imaging in the analysis position, ion imaging of Pb^+ and U^+ was found to be an essential prerequisite for locating the zirconolites and targeting the probe (e.g., Fig. 6b, d and f). Each analysis

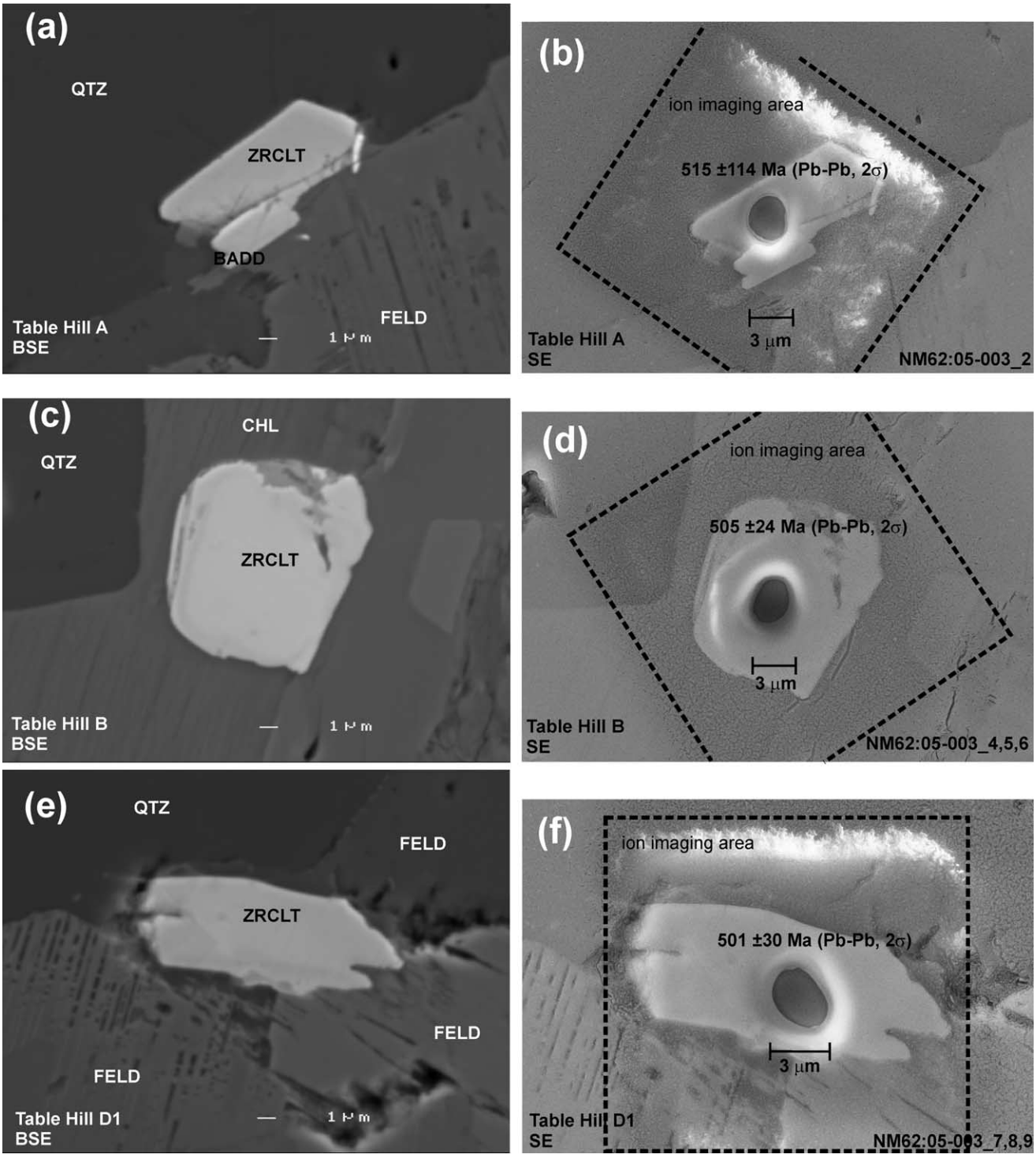

Fig. 6. Paired backscattered electron (before) and secondary electron (after) images of representative zirconolite grains from Th1 dolerite sill analyzed in situ. The pits remaining from the NanoSIMS analyses are clearly visible, and the mean $^{207}Pb^*/^{206}Pb^*$ ages and uncertainties are shown. (b), (d), and (f) also show the outlined regions of ion imaging conducted prior to analysis for targeting the probe spot. Abbreviations—ZRCLT: zirconolite, BADD: baddeleyite; QTZ: quartz; CHL: chlorite; FELD: feldspar.

was 35 min in duration. For grains B and D_1, the first analysis was immediately followed by two replicates from the same location, yielding a total of nine analyses. Additional replicates could not be acquired because the ion beam penetrated through these platy, ~1 μm thick grains in 1.5 h (Fig. 6d and f).

The mean count rate for ^{206}Pb was ~700 ± 400 cps, and based upon the Pb sensitivity determined for zirconolite

Table 2
NanoSIMS Pb-isotope data for zirconolite grains, dolerite sill, Table Hill Volcanics, South Australia

Analysis #	Sample name	$^{204}Pb/^{206}Pb$[a]	$^{207}Pb/^{206}Pb$	$\pm 2\sigma$	$^{208}Pb/^{206}Pb$	$\pm 2\sigma$	$^{207}Pb^*/^{206}Pb^*$[b]	$\pm 2\sigma$	$^{207*}Pb/^{206*}Pb$ age (Ma)	$\pm 2\sigma$
05-003_1	D2	1.4E-04	0.0580	0.0025	2.047	0.092	0.0559	0.0036	448	143
05-003_2	A	2.8E-04	0.0606	0.0013	2.750	0.140	0.0576	0.0030	515	114
05-003_3	C	1.3E-03	0.0841	0.0097	1.688	0.065	0.0620	0.0053	674	183
05-003_4	B	7.7E-05	0.0581	0.0008	0.915	0.018	0.0574	0.0009	507	36
05-003_5	B replicate	4.4E-05	0.0590	0.0016	0.866	0.023	0.0584	0.0019	545	71
05-003_6	B replicate	7.1E-05	0.0584	0.0009	0.880	0.026	0.0570	0.0010	492	38
05-003_7	D_1	6.8E-05	0.0582	0.0015	1.342	0.043	0.0575	0.0023	511	88
05-003_8	D_1 replicate	1.1E-04	0.0571	0.0009	1.256	0.040	0.0563	0.0017	464	67
05-003_9	D_1 replicate	8.8E-06	0.0578	0.0010	1.296	0.045	0.0575	0.0010	511	38

[a] Median value as an indication only.
[b] Corrected for common Pb at 500 Ma and composition of [25].

(see above), the ^{206}Pb and ^{207}Pb contents in the zirconolite are estimated to have been $\sim 550 \pm 300$ ppm (wt.) and ~ 30 ppm, respectively. The $^{208}Pb/^{206}Pb$ values ranged from 0.86 to 2.75, giving model Th/U of 3–9 based on the mean age (below); small variations in $^{208}Pb/^{206}Pb$ between replicates (Table 2) may reflect compositional zoning with depth. The mean U and Th contents are calculated at 0.8 and 4 wt.%, respectively. The individual 2σ precision in the raw $^{207}Pb/^{206}Pb$ ratios ranged from 1.5 to 11.5%. The median $^{204}Pb/^{206}Pb$ value was 9.44×10^{-5}. After common Pb correction, the individual $^{207}Pb^*/^{206}Pb^*$ age precision ranged from 7 to 32%. The mean $^{207}Pb^*/^{206}Pb^*$ age of all nine analyses, uncorrected for IMF, is 504 ± 18 Ma (MSWD = 0.89). Assuming an IMF of −0.1%, the calculated age would be 506 Ma. Either result is within error of the 500.1 ± 7.4 Ma K–Ar age mentioned previously, and consistent with regional geochronological constraints.

5. Conclusions

The NanoSIMS 50 ion microprobe proved to be a capable performer in conducting Pb-isotope geochronology at a lateral scale of ∼3 μm. The secondary mass analyzer could be tuned to the standards of mass resolution (i.e., $M/\Delta M \sim 5000$) and quality (i.e., flat-topped) that are now the norm for ion probe Pb-isotope geochronology, although this required significant truncation of the secondary ion beam. The sensitivity for Pb^+ proved adequate for the analysis of moderate to high-U minerals such as xenotime, zirconolite and uraninite. For the analysis of other minerals with lower U contents, such as zircon and baddeleyite, there remains a strong case for using the large-geometry ion probes that have Pb^+ sensitivity values 3–4× those of the NanoSIMS. A ^{207}Pb content of 10 ppm (wt.) is suggested as the minimum for $^{207}Pb^*/^{206}Pb^*$ dating to be of practical utility at the 3 μm scale. The analysis of some mineral Pb-isotope reference materials indicated that instrumental mass fractionation (IMF) could be a factor, but these findings were inconsistent with measurements of Pb-metal standards which indicated undetectable IMF. Further work is required to determine the origin of this discrepancy, including factors such as sample mount position.

The $^{207}Pb^*/^{206}Pb^*$ age obtained for small zirconolite grains from a Cambro-Ordovician intrusive rock from Australia were used to illustrate the potential applications of high-spatial-resolution in situ geochronology. Our ongoing studies indicate that determining the $^{206}Pb/^{238}U$ or $^{208}Pb/^{232}Th$ ratios is comparatively straightforward, and can be accomplished in static multicollection mode in sequence with the Pb-isotope measurements. A key factor in the reproducibility of the $^{206}Pb/^{238}U$ or $^{208}Pb/^{232}Th$ ratios will be controlling the instrument tuning between analyses, particularly centering the secondary beam within the very narrow entrance slit.

The utility of small-spot U–Th–Pb geochronology is limited by the Pb and U concentrations in the mineral, the sensitivity of the technique, the precision required, as well as other practical considerations. We found that it was not possible with the NanoSIMS to achieve suitably high secondary ion currents to make useful geochronological analyses at a scale <3 μm for any but the most Pb-rich materials. Primary beam current is one impediment, with a 1 μm diameter $^{16}O^-$ probe containing a primary current of only 10–15 pA, too low to generate useful Pb^+ beams in most minerals. Future improvements to oxygen ion beam density, as well as the duty cycle, through the use of a detector array capable of analyzing the Pb-isotopes simultaneously, may allow ion probe U–Th–Pb geochronology to become practical at the ∼1 μm lateral scale.

Acknowledgements

The authors acknowledge the technical, scientific and financial (TAP Grant #4003 to NJM) assistance from the Nanostructural Analysis Network Organisation Major National Research Facility (NANO-MNRF). François Hillion and an anonymous journal referee provided valuable comments on the manuscript. Frank J. Stadermann (Washington University, St. Louis) kindly provided his NanoSIMS ion optics diagram for Fig. 1.

References

[1] C.A. Andersen, J.R. Hinthorne, Earth Planet. Sci. Lett. 14 (1972) 195.
[2] J.R. Hinthorne, C.A. Andersen, R.L. Conrad, J.F. Lovering, Chem. Geol. 25 (1979) 271.
[3] W. Compston, I.S. Williams, C. Meyer, J. Geophys. Res. 89 (1984) 525.
[4] T. Ireland, I.S. Williams, Rev. Mineral. Geochem. 53 (2003) 215.
[5] N.J. McNaughton, B. Rasmussen, I.R. Fletcher, Science 285 (1999) 78.
[6] D.A. Vallini, B. Rasmussen, B. Krapez, I.R. Fletcher, N.J. McNaughton, Geol. 30 (2002) 1083.
[7] N. Kositcin, N.J. McNaughton, B.J. Griffin, I.R. Fletcher, D.I. Groves, B. Rasmussen, Geochim. Cosmochim. Acta 67 (2003) 709.
[8] I.R. Fletcher, B. Rasmussen, N.J. McNaughton, Aust. J. Earth Sci. 47 (2000) 845.
[9] B. Rasmussen, I.R. Fletcher, N.J. McNaughton, Geology 29 (2001) 963.
[10] T.J. Dempster, D.C. Hay, B.J. Bluck, Geology 32 (2004) 221.
[11] B. Rasmussen, I.R. Fletcher, Geology 32 (2004) 785.
[12] C.J. Carson, R.G. Berman, R.A. Stern, M. Sanborn-Barrie, T. Skulski, H.A.I. Sandeman, Can. J. Earth Sci. 41 (2004) 1049.
[13] C.J. Carson, J.J. Ague, M. Grove, C.D. Coath, T.M. Harrison, Earth Planet. Sci. Lett. 199 (2002) 287.
[14] C.M. Breeding, J.J. Ague, M. Grove, A.L. Rupke, Am. Mineral. 89 (2004) 1067.
[15] M. Grove, T.M. Harrison, Geology 27 (1999) 487.
[16] G. Slodzian, B. Daigne, F. Girard, F. Boust, F. Hillion, Biol. Cell 74 (1992) 53.
[17] F. Hillion, B. Daigne, F. Girard, G. Slodzian, in: A. Benninghoven, Y. Nihei, N. Shimizu, H.W. Werner (Eds.), Secondary Ion Mass Spectrometry, SIMS IX, Wiley, 1994, p. 254.
[18] P. Hoppe, New Astro. Rev. 46 (2002) 589.
[19] A. Benninghoven, F.G. Rudenauer, H.W. Werner, Secondary Ion Mass Spectrometry, Basic Concepts, Instrumental Aspects, Applications and Trends, Wiley, New York, 1987.
[20] H. Liebl, Vacuum 22 (1972) 619.
[21] A.D. McNaught, A. Wilkinson, Compendium of Chemical Terminology, The Gold Book, 2nd ed., Blackwell Science, 1997.
[22] G. Slodzian, M. Chaintreau, R. Dennebouy, A. Rousse, Eur. Phys. J. -Appl. Phys. 14 (2001) 199.
[23] R.A. Stern, I. Fletcher, N.J. McNaughton, B. Griffin, SHRIMP Workshop, Hiroshima, Japan, 2004, p. 48.
[24] K.R. Ludwig, http://www.bgc.org/klprogrammenu.html, 2001.
[25] J.S. Stacey, J.D. Kramers, Earth Planet. Sci. Lett. 26 (1975) 207.
[26] R.M. Hocking, Western Australia Geological Survey Record 1994/4, 1994.
[27] E.J. Catanzaro, T.J. Murphy, W.R. Shields, E.L. Garner, J. Res. Natl. Bur. Stand. Technol. 72A (1968) 261.
[28] R. Doucelance, G. Manhes, Chem. Geol. 176 (2001) 361.
[29] M.F. Thirlwall, Chem. Geol. 184 (2002) 255.
[30] R.A. Stern, N. Rayner, W. Davis, Y. Amelin, I.R. Annesley, T. Bonli, 12th Annual V.M. Goldschmidt Conference, Cambridge Publications Davos, Switzerland, 2002, pp. A741.
[31] R.A. Stern, N. Rayner, Curr. Res., Radiogenic Age and Isotopic Studies: Report 16, Geological Survey of Canada, 2003.
[32] V.M. Oversby, A.E. Ringwood, Radioact. Waste Manag. 1 (1981) 289.
[33] J.J. Veevers, Earth Sci. Rev. 68 (2004) 1.
[34] M.H. Dodson, J. Sci. Instrum. 40 (1963) 290.
[35] N. Shimizu, S.R. Hart, J. Appl. Phys. 53 (1982) 1303.